

MILLIMETER EMISSION STRUCTURE IN THE FIRST ALMA IMAGE OF THE AU Mic DEBRIS DISK

MEREDITH A. MACGREGOR¹, DAVID J. WILNER¹, KATHERINE A. ROSENFELD¹, SEAN M. ANDREWS¹,
BRENDA MATTHEWS², A. MEREDITH HUGHES³, MARK BOOTH^{2,4}, EUGENE CHIANG³,
JAMES R. GRAHAM^{3,5}, PAUL KALAS^{3,6}, GRANT KENNEDY⁷, AND BRUCE SIBTHORPE⁸

¹ Harvard-Smithsonian Center for Astrophysics, 60 Garden Street, Cambridge, MA 02138, USA

² Herzberg Institute of Astrophysics, 5072 West Saanich Road, Victoria, BC V9E 2E7, Canada

³ Department of Astronomy, 601 Campbell Hall, University of California, Berkeley, CA 94720, USA

⁴ Department of Physics & Astronomy, University of Victoria, 3800 Finnerty Rd., Victoria, BC V8P 5C2, Canada

⁵ Dunlap Institute for Astronomy & Astrophysics, University of Toronto, Toronto, ON, Canada

⁶ SETI Institute, 189 Bernardo Ave., Mountain View, CA 94043, USA

⁷ Institute of Astronomy, University of Cambridge, Madingley Road, Cambridge CB3 0HA, UK

⁸ SRON Netherlands Institute for Space Research, NL-9747 AD Groningen, The Netherlands

Received 2012 November 9; accepted 2012 November 17; published 2012 December 17

ABSTRACT

We present 1.3 mm ALMA Cycle 0 observations of the edge-on debris disk around the nearby, ~ 10 Myr old, M-type star AU Mic. These observations obtain $0''.6$ (6 AU) resolution and reveal two distinct emission components: (1) the previously known dust belt that extends to a radius of 40 AU and (2) a newly recognized central peak that remains unresolved. The cold dust belt of mass $\sim 1 M_{\text{Moon}}$ is resolved in the radial direction with a rising emission profile that peaks sharply at the location of the “birth ring” of planetesimals hypothesized to explain the midplane scattered light gradients. No significant asymmetries are discerned in the structure or position of this dust belt. The central peak identified in the ALMA image is ~ 6 times brighter than the stellar photosphere, which indicates an additional emission process in the inner regions of the system. Emission from a stellar corona or activity may contribute, but the observations show no signs of temporal variations characteristic of radio-wave flares. We suggest that this central component may be dominated by dust emission from an inner planetesimal belt of mass $\sim 0.01 M_{\text{Moon}}$, consistent with a lack of emission shortward of $25 \mu\text{m}$ and a location $\lesssim 3$ AU from the star. Future millimeter observations can test this assertion, as an inner dust belt should be readily separated from the central star at higher angular resolution.

Key words: circumstellar matter – planet–disk interactions – stars: individual (AU Microscopii) – submillimeter: planetary systems

Online-only material: color figures

1. INTRODUCTION

Debris disks are created by the collisional erosion of planetesimals, the building blocks of planetary systems. These collisions continuously generate dust grains with a range of sizes that are detected with astronomical measurements from optical to radio wavelengths. Resolved observations of nearby debris disks are instrumental in advancing our understanding of these systems. At a distance of 9.91 ± 0.10 pc (van Leeuwen 2007), the M1 star AU Mic hosts one of the closest and best studied debris disks. The detection of submillimeter emission (Liu et al. 2004) from this ~ 10 Myr old system in the β Pic moving group (Zuckerman et al. 2001) was followed quickly by the discovery of an edge-on disk seen in scattered starlight (Kalas et al. 2004). Subsequent work has characterized the scattered light in great detail, exploiting its proximity to constrain its radial and vertical structure (Liu 2004; Krist et al. 2005; Metchev et al. 2005; Graham et al. 2007; Fitzgerald et al. 2007).

Observations of dust emission at (sub)millimeter wavelengths provide important, complementary information about debris disk structures. Unlike the small grains probed at optical and near-infrared wavelengths that react strongly to stellar radiation and wind forces, the large grains that dominate the millimeter-wave emission have dynamics more like the parent planetesimals. As a result, long-wavelength images trace best the location and distribution of the larger colliding bodies (Wyatt 2006), and potentially also the signatures of planets that

interact with them (Ertel et al. 2012). These size-dependent dust dynamics manifest beautifully in the edge-on AU Mic disk. Resolved millimeter-wave observations show an emission belt within the extended optical disk that peaks near a radius of 35 AU, where the midplane scattered light profile steepens dramatically (Wilner et al. 2012). These features are elegantly explained by the presence of a “birth ring” of planetesimals at that location, where small grains released in a collisional cascade are launched into an extended halo (Strubbe & Chiang 2006; Augereau & Beust 2006).

With the advent of the Atacama Large Millimeter Array (ALMA), the millimeter emission in nearby debris disks can be imaged in much greater detail (e.g., Boley et al. 2012). In this Letter, we present new, subarcsecond resolution ALMA Cycle 0 observations of AU Mic at $\lambda = 1.3$ mm. The ALMA data provide substantially improved constraints on the locations of colliding planetesimals in the AU Mic disk and help shed light on the processes that may be shaping the planetesimal distribution. They also reveal a previously unknown, centrally located emission feature.

2. OBSERVATIONS

AU Mic was observed by ALMA with its Band 6 receivers over four 2 hr long “scheduling blocks” (SBs) in 2012 April and June. Table 1 summarizes the observations. The 16–20 operational 12 m antennas were arranged to span baseline lengths of

Table 1
ALMA Cycle 0 Observations of AU Mic

ID	Date (UT)	Antennas	PWV (mm)
SB-1	2012 Apr 23 07:30–09:26	17	1.7
SB-2	2012 Apr 23 09:39–11:03	16	1.7
SB-3	2012 Apr 24 09:09–11:19	18	3.0
SB-4	2012 Jun 16 05:48–08:02	20	0.7

21–402 m (corresponding to a maximum resolution of $\sim 0''.6$). The correlator was configured to optimize continuum sensitivity, processing two polarizations in four 2 GHz-wide basebands, each with 128 spectral channels, centered at 226, 228, 242, and 244 GHz. In each SB, we interleaved observations of AU Mic (pointing center $\alpha = 20^{\text{h}}45^{\text{m}}09^{\text{s}}.34$, $\delta = -31^{\circ}20'24''.09$, J2000, within $1''$ of the star position at all epochs) with the nearby quasar J2101–295.

The data from each SB were calibrated independently within the CASA software package. After applying system temperature measurements and phase corrections from the water vapor radiometers, the data were flagged and averaged into 6.048 s integrations. A calibration of the spectral response of the system was determined from observations of J1924–292, and complex gain variations induced by atmospheric and instrumental effects were corrected using observations of J2101–295. The absolute flux calibration was derived from observations of Neptune: a mean calibration was applied to all basebands, with a systematic uncertainty of $\sim 10\%$ (see Section 3.3). To generate an image at the mean frequency, 235 GHz (1.28 mm), we Fourier inverted the calibrated visibilities with natural weighting and performed a multi-frequency synthesis deconvolution with the CLEAN algorithm. The visibilities were further reduced by spectrally averaging over the central 112 channels in each baseband and re-weighted by the observed scatter.

3. RESULTS AND ANALYSIS

3.1. Image of 1.3 mm Dust Continuum Emission

Figure 1 shows an image of the $\lambda = 1.3$ mm emission from SB-4 (with the most antennas and best weather conditions), with synthesized beam $0''.80 \times 0''.69$ (8×7 AU), position angle (P.A.) 49° , and an rms of $30 \mu\text{Jy beam}^{-1}$. An image constructed from all four SBs is consistent but noisier, which we attribute to systematic calibration issues resulting from the poorer weather conditions of the earlier observations. The emission is confined to a narrow band with an aspect ratio $> 10:1$, with an orientation consistent with the scattered light disk. The emission is not resolved in the direction perpendicular to the elongation. There are clear peaks near both extrema and in the middle of the structure (detected at all four epochs). The emission is marginally brighter at the northwest end than the southeast end, and shows small undulations along its length, though none of these variations are significant. We interpret the observed structure as a superposition of two components: (1) the nearly edge-on dust belt with limb-brightened ansae and (2) a new, distinct, and compact feature located at the center of the belt.

3.2. Modeling Formalism

Building on the phenomenological methodology of Wilner et al. (2011, 2012) to analyze resolved millimeter emission from debris disks, we construct a parametric model to quantify

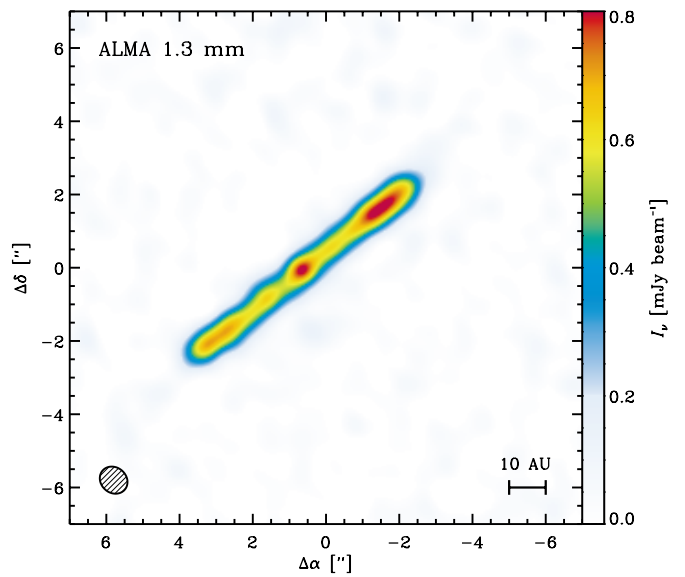


Figure 1. ALMA image of the 1.3 mm continuum emission from AU Mic. The ellipse in the lower left corner represents the $0''.80 \times 0''.69$ (8×7 AU) synthesized beam.

(A color version of this figure is available in the online journal.)

the observed properties of the AU Mic emission. We consider two model components: a vertically thin, axisymmetric “outer” belt and an additional source to account for the central peak. The belt component is informed by models of the scattered light that show the disk midplane within 50 AU is remarkably straight, $\lesssim 0.5^\circ$ from edge-on, and thin (FWHM $\sim 0''.3$). We assume that the belt is viewed at an inclination of 89.5° . The belt is characterized as an annulus with (unprojected) radial intensity $I_v(r) \propto r^x$ for $r_i < r < r_o$, with a normalization defined by $F_{\text{belt}} = \int I_v d\Omega$, a center determined by offsets (relative to the pointing center) $\{\Delta\alpha, \Delta\delta\}$, and an orientation described by a P.A. We treat the central component as a circular Gaussian with mean Δr_{cen} , variance σ_{cen}^2 (half-width at half-maximum $R_{\text{cen}} = \sqrt{2 \ln 2} \sigma_{\text{cen}}$), and flux density F_{cen} . The mean Δr_{cen} is defined as a radial shift from the belt center *in the plane of the belt*. We also include power-law spectral scalings between the four basebands for each component, denoted α_{belt} and α_{cen} , where $F_\nu \propto \nu^\alpha$.

For a given parameter set, we compute four synthetic visibility sets sampled at the same spatial frequencies observed by ALMA, corresponding to the spectrally averaged basebands (at 226, 228, 242, and 244 GHz). By fitting the visibility data directly, we are not sensitive to the non-linear effects of deconvolution, and take advantage of the full range of available spatial frequencies. The fit quality is quantified by a likelihood metric, \mathcal{L} , determined from the χ^2 values summed over the real and imaginary components at all spatial frequencies ($\ln \mathcal{L} = -\chi^2/2$). A Monte Carlo Markov Chain (MCMC) approach was utilized to characterize the multi-dimensional parameter space of this model and determine the posterior probability distribution functions for each parameter. We used the affine-invariant ensemble sampler proposed by Goodman & Weare (2010), in a locally modified version of the parallelized implementation described by Foreman-Mackey et al. (2012), to compute likelihood values for $\sim 10^6$ MCMC trials. Uniform priors were assumed for all parameters, with bounds imposed to ensure that the model was well defined: $\{F_{\text{belt}}, F_{\text{cen}}, \sigma_{\text{cen}}^2\} \geq 0$, and $0 \leq r_i < r_o$.

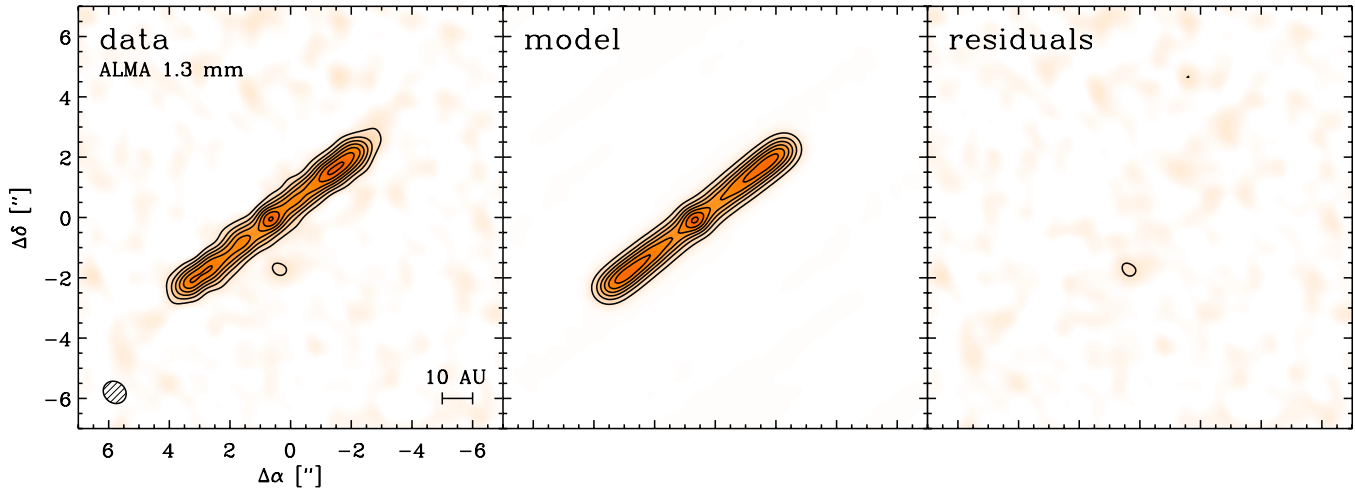


Figure 2. Left: the observed 1.3 mm emission from AU Mic. Center: the best-fit model (see Section 3.3). Right: the imaged residuals. Contours are drawn at 4σ ($120 \mu\text{Jy beam}^{-1}$) intervals.

(A color version of this figure is available in the online journal.)

Table 2
Model Parameters

Parameter	Description	Best-Fit	68% Confidence Interval
F_{belt}	Belt flux density (mJy)	7.14	+0.12, -0.25
x	Belt radial power law index	2.32	+0.21, -0.31
r_i	Belt inner radius (AU)	8.8	+11.0, -1.0
r_o	Belt outer radius (AU)	40.3	+0.4, -0.4
P.A.	Belt position angle ($^\circ$)	128.41	+0.12, -0.13
α_{belt}	Belt spectral index	-0.15	+0.40, -0.58
F_{cen}	Gaussian flux density (mJy)	0.32	+0.06, -0.06
Δr_{cen}	Gaussian offset (AU)	0.71	+0.35, -0.51
σ_{cen}^2	Gaussian variance (AU^2)	≤ 5.9	(3σ limit)
α_{cen}	Gaussian spectral index	-0.35	+2.1, -4.5
$\Delta\alpha$	R.A. offset of belt center (")	0.61	+0.02, -0.02
$\Delta\delta$	Decl. offset of belt center (")	-0.03	+0.02, -0.02

3.3. Results of Model Fits

The best-fit parameter values and their 68% uncertainties determined from the marginalized posterior probability distributions are listed in Table 2. The data and best-fit model are compared in the image plane in Figure 2; there are no significant residuals. The best-fit model has a reduced $\chi^2 = 1.37$ (905, 920 independent data points, 12 free parameters). The modeling procedure was performed on each SB individually and the full data set (all four SBs together). The results were entirely consistent, although the parameter uncertainties were notably smaller from the superior SB-4 data set alone, and we focus on those results.

Most parameters are determined with high precision. We find good agreement of the outer belt parameters $\{F_{\text{belt}}, r_i, r_o\}$ with the less well-constrained fits of Wilner et al. (2012), and on the disk P.A. from measurements of scattered starlight (e.g., Krist et al. 2005). We measure a flat spectrum for the outer belt ($\alpha_{\text{belt}} \approx 0$) across the four basebands, which corresponds to the difference between the spectral slopes of AU Mic and Neptune ($\alpha_{\text{Neptune}} \approx 2.1$), consistent with data from 350 μm to 1.3 mm (Wilner et al. 2012).

The central emission peak is detected with high confidence at $F_{\text{cen}} = 320 \mu\text{Jy}$ ($>10\sigma$ brighter than the outer belt at that location). It is unresolved, with $R_{\text{cen}} \leq 3.0 \text{ AU}$ (3σ), and

positionally coincident with the outer belt center: $\Delta r_{\text{cen}} \leq 1.9 \text{ AU}$ (3σ). Regarding the outer belt, the most notable result is that the models strongly favor rising emission profiles with large, positive gradients: $x \approx 2.3 \pm 0.3$. Models with the standard assumption of $x < 0$ produce significant residuals, underpredicting the intensities at $\pm 1''$ – $2''$ from the belt center. Because of the steep increase in the emission profile, there is only a weak constraint on the inner edge of the outer belt. The best-fit r_i deviates from 0 at the $\sim 2\sigma$ level: the 3σ limit is $r_i \leq 21 \text{ AU}$.

4. DISCUSSION

We have presented new, subarcsecond resolution ALMA observations of 1.3 mm emission from the AU Mic debris disk and analyzed the data with a simple parametric model. This emission is resolved into two distinct components: (1) an edge-on outer belt with an emission profile that rises with radius out to 40 AU, and (2) an unresolved peak at the center of the outer belt. This distribution is more complex than the single, narrow ring often assumed for debris disks. However, it has some similarities to other nearby resolved systems, such as ϵ Eri (Backman et al. 2009) or HR 8799 (Su et al. 2009), that show an inner component inferred from excess infrared emission, separate from an extended and colder outer belt.

4.1. The Central Emission Peak

The stellar photosphere is much fainter than the central peak noted in Figure 1. A NextGen stellar model (Hauschildt et al. 1999) with $T_{\text{eff}} = 3720 \text{ K}$, $L_* = 0.11 L_\odot$, and $M_* = 0.6 M_\odot$ (e.g., Metchev et al. 2005; Chen et al. 2005) that matches the AU Mic photometry from 0.4 to 25 μm contributes only $F_* = 52 \mu\text{Jy}$ at 1.3 mm, ~ 6 times fainter than observed. However, AU Mic is an active star that exhibits radio-wave bursts. In quiescence, observations find $<120 \mu\text{Jy}$ at 3.6 cm (White et al. 1994), and the contribution at 1.3 mm from hot coronal plasma seen in X-rays is unlikely to be significant (though better spectral constraints are desirable; see Leto et al. 2000). Flares are detected from AU Mic at ~ 200 – $1200 \mu\text{Jy}$ at 6 cm (Bower et al. 2009), but this non-thermal emission is much weaker at 1.3 mm. While the unknown variability makes any extrapolation to 1.3 mm problematic, the temporal properties

of the ALMA emission provide additional information. Radio-wave flares have fast decay times, of the order of an hour (Kundu et al. 1987); but, the mm-wave peak persists at a consistent intensity in all four ALMA observations, within uncertainties that are typically 2–3 times larger than for SB-4, spanning timescales from 1 hr (within SB-4) to two months (SB-1 to SB-4). Unfortunately, the spectral index (α_{cen}) constraints are not good enough to be diagnostic. We suspect that stellar emission is too weak and too ephemeral to be responsible for the 1.3 mm peak, but the available data do not allow for a firm determination of its contribution.

Alternatively, the central emission peak could be produced by dust in a distinct (unresolved) planetesimal belt located close to the star. In Section 3.3, we constrained the extent of this peak to $\mathcal{R}_{\text{cen}} \leq 3$ AU (3σ), inside the inner working angle ($0''.8 \approx 8$ AU) of all previous high-resolution imaging of scattered light (Krist et al. 2005; Fitzgerald et al. 2007). Rough models of the spectral energy distribution (SED) from the ALMA central peak can help assess the feasibility that it originates in an inner dust belt. In this context, the most salient feature of the AU Mic SED is the absence of emission excess at $\lambda \leq 25 \mu\text{m}$ (e.g., Liu et al. 2004; Chen et al. 2005). We assume the central peak represents the combined emission from the star and dust, such that $F_{\text{dust}} = F_{\text{cen}} - F_* \approx 0.25$ mJy at 1.3 mm. Optically thin dust emission at a temperature, T , has $F_{\text{dust}} \approx \kappa_{\nu} B_{\nu}(T) M_{\text{dust}}/d^2$, where κ_{ν} is the opacity spectrum, B_{ν} the Planck function, M_{dust} is the dust mass, and $d = 9.91$ pc. For a given dust population characterized by κ_{ν} , we computed the maximum T (and minimum M_{dust}) consistent with both the observed millimeter flux density and the infrared SED. We calculated various κ_{ν} for dust with the Weingartner & Draine (2001) “astrosilicate” composition and a power-law size distribution $n(a) \propto a^{-3.5}$ between $a_{\text{min}} = 0.2 \mu\text{m}$ (the blowout size; Strubbe & Chiang 2006) and a_{max} values from 1 μm to 1 cm. For $a_{\text{max}} \leq 100 \mu\text{m}$, models of the central peak overpredict the observed 60–70 μm emission if $T > 35$ K. However, larger grains with $a_{\text{max}} \geq 1$ mm at temperatures up to $T \approx 75$ K can be accommodated without producing an excess at $\lambda \leq 25 \mu\text{m}$. These maximum T values are comparable to the expected dust temperatures a few AU from the star, compatible with the emission size constraints (\mathcal{R}_{cen}). The corresponding minimum M_{dust} is $\sim 9 \times 10^{23}$ g, about 1% of the lunar mass. These calculations show that the central emission peak is consistent with a cool dust belt located $\lesssim 3$ AU from the central star, with a total mass comparable to the asteroid belt in our solar system. If this interpretation is correct, then ALMA observations at higher resolution can determine its properties. Interestingly, the temperature of this putative inner belt is colder than the ~ 190 K found to apply systematically to inner belts around F5-K0 stars by Morales et al. (2011).

4.2. The Outer Dust Belt

Our modeling of the ALMA data locates the far edge of the outer emission belt with high precision, $r_o = 40$ AU, which matches closely the outer edge of the hypothesized “birth ring” of colliding planetesimals. This analysis does not define the shape of the edge below the ~ 6 AU resolution limit, but the truncation is reminiscent of the outer edge of the classical Kuiper Belt (47 ± 1 AU; Trujillo & Brown 2001). The origins of such sharp edges remain unclear: they could be from dynamical interactions (Ida et al. 2000; Boley et al. 2012), or they may simply represent the initial conditions, where planetesimal formation was efficient and successful in the primordial disk.

Adopting the opacity used in Section 4.1 ($\kappa_{\nu} = 2.7 \text{ cm}^2 \text{ g}^{-1}$), and assuming $T \approx 25$ K (for 35–45 AU), the dust mass of this outer belt is 7×10^{25} g (consistent with previous estimates; Liu et al. 2004), ~ 100 times more massive than the hypothesized inner belt; the Kuiper Belt and asteroid belt have a similar mass ratio.

The mm-wave emission morphologies of cold belts of dusty debris reflect the dynamical processes that shape the underlying planetesimal distributions. For AU Mic, our modeling suggests that its outer emission belt can be described by an increasing emission profile with a positive radial power-law index $x \approx 2.3 \pm 0.3$. If we assume the emitting dust is in radiative equilibrium with a temperature profile $T \propto r^{-0.5}$, this implies a rising surface density profile, $\Sigma \propto r^{2.8}$, strongly peaked near 40 AU. A broad parent body ring with constant surface density would produce a radial intensity profile with $x \approx -0.5$, a value ruled out with high confidence ($>5\sigma$). A rising behavior is predicted for “self-stirred” disks with ongoing planet formation (Kenyon & Bromley 2002); in particular, the models of Kennedy & Wyatt (2010) suggest $\Sigma \propto r^{7/3}$. However, the timescale required to assemble Pluto-sized bodies at ~ 40 AU to initiate a collisional cascade around a low-mass star like AU Mic is much longer than its ~ 10 Myr age (Kenyon & Bromley 2008). Moreover, this scenario does not naturally accommodate the presence of a separate, interior planetesimal belt. Of course, the still modest resolution of the data is compatible with more complex scenarios, such as multiple closely spaced belts of different brightnesses that mimic a smooth gradient. Scattered light observations of the AU Mic disk show asymmetries on both large and small scales, with several peaks and depressions projected against the broad ansae in Figure 1, at radii beyond the millimeter undulations (features A–E; see Fitzgerald et al. 2007). With such a steep emission gradient in this outer belt, the data do not strongly constrain its width, or the location of its inner edge. Our modeling indicates substantial emission from mm sized grains interior to 40 AU, in the ~ 20 –40 AU zone inferred to be highly depleted of μm sized grains from polarized scattered light (Graham et al. 2007).

The ALMA data show no clear evidence for asymmetries or substructure that would signal planet–disk interactions. The hints of modulating millimeter brightness along the belt in Figure 1 are insignificant in the residuals from subtracting a symmetric parametric model (see Figure 2). This rules out substructure brighter than $90 \mu\text{Jy beam}^{-1}$ (3σ), corresponding to dust clumps $\gtrsim 1\%$ of the lunar mass (for the dust properties adopted above). Those limits argue against overdensities of dust-producing planetesimals trapped in mean motion resonances (Kuchner & Holman 2003), as might arise from the outward migration of planets (Wyatt 2003). Given the young age of the system, the broad and smooth character of the outer belt in the AU Mic disk may resemble the Kuiper Belt prior to the epoch of Neptune’s migration (Malhotra 1995). It is interesting that none of the claims of millimeter emission clumps in debris disks have survived scrutiny at higher sensitivity (Piétu et al. 2011; Hughes et al. 2011, 2012). It may be that any such features are effectively erased by collisions (Kuchner & Stark 2010). We also find no significant centroid offset between the outer belt and central peak, as might result from the secular perturbations of a planet in an eccentric orbit (Wyatt et al. 1999). The limit on the displacement, $\Delta r_{\text{cen}} < 1.9$ AU (3σ), corresponds approximately to a limit on ae , where a is the semimajor axis and e is the eccentricity. This limit can still accommodate a wide-orbit planet with modest eccentricity, similar to Uranus. Such a planet

could be responsible for stirring the disk to 40 AU in ~ 10 Myr (e.g., for $a = 30$ AU and $e = 0.05$, see Equation (15) of Mustill & Wyatt 2009). Limits from high contrast direct imaging admit Saturn-mass planets at these separations (Delorme et al. 2012).

4.3. Concluding Remarks

The basic architecture of the AU Mic debris disk appears remarkably similar to the solar system, with a potential analog to the asteroid belt at a few AU, and a colder, more massive, and apparently truncated counterpart of the Kuiper Belt extending to 40 AU. Future observations are needed to determine if stellar processes could be responsible for emission attributed to the asteroid belt, and to determine if the solar system analogy extends to include a planetary system like our own.

M.A.M. thanks NRAO for Student Observing Support funds. A.M.H. is supported by a fellowship from the Miller Institute for Basic Research in Science. M.B. is funded through a Space Science Enhancement Program grant from the Canadian Space Agency and an NSERC Discovery Accelerator Supplement. E.C. acknowledges NSF grant AST-0909210. P.K. and J.R.G. acknowledge support from NSF Award 0909188 and NASA Award NNX11AD21G. This Letter makes use of the following ALMA data: ADS/JAO.ALMA#2011.0.00142.S. ALMA is a partnership of ESO (representing its member states), NSF (USA), and NINS (Japan), together with NRC (Canada) and NSC and ASIAA (Taiwan), in cooperation with the Republic of Chile. The Joint ALMA Observatory is operated by ESO, AUI/NRAO, and NAOJ. The National Radio Astronomy Observatory is a facility of the National Science Foundation operated under cooperative agreement by Associated Universities, Inc.

Facility: ALMA

REFERENCES

- Augereau, J.-C., & Beust, H. 2006, *A&A*, 455, 987
 Backman, D., Marengo, M., Stapelfeldt, K., et al. 2009, *ApJ*, 690, 1522
 Boley, A. C., Payne, M. J., Corder, S., et al. 2012, *ApJL*, 750, 21
 Bower, G. C., Bolatto, A., Ford, E. B., & Kalas, P. 2009, *ApJ*, 701, 1922
 Chen, C. H., Patten, B. M., Werner, M. W., et al. 2005, *ApJ*, 634, 1372
 Delorme, P., Lagrange, A. M., Chauvin, G., et al. 2012, *A&A*, 539, 72
 Ertel, S., Wolf, S., & Rodmann, J. 2012, *A&A*, 544, A61
 Fitzgerald, M. P., Kalas, P. G., Duchêne, G., Pinte, C., & Graham, J. R. 2007, *ApJ*, 670, 536
 Foreman-Mackey, D., Hogg, D. W., Lang, D., & Goodman, J. 2012, arXiv:1202.3665
 Goodman, J., & Weare, J. 2010, *Commun. Appl. Math. Comput. Sci.*, 5, 65
 Graham, J. R., Kalas, P. G., & Matthews, B. C. 2007, *ApJ*, 654, 595
 Hauschildt, P. H., Allard, F., & Baron, E. 1999, *ApJ*, 512, 377
 Hughes, A. M., Wilner, D. J., Andrews, S. M., et al. 2011, *ApJ*, 740, 38
 Hughes, A. M., Wilner, D. J., Mason, B., et al. 2012, *ApJ*, 750, 82
 Ida, S., Larwood, J., & Burkert, A. 2000, *ApJ*, 528, 351
 Kalas, P., Liu, M. C., & Matthews, B. C. 2004, *Sci*, 303, 1990
 Kennedy, G. M., & Wyatt, M. C. 2010, *MNRAS*, 405, 1253
 Kenyon, S. J., & Bromley, B. C. 2002, *ApJL*, 577, 35
 Kenyon, S. J., & Bromley, B. C. 2008, *ApJS*, 179, 451
 Krist, J. E., Ardila, D. R., Golimowski, D. A., et al. 2005, *AJ*, 129, 1008
 Kuchner, M. J., & Holman, M. J. 2003, *ApJ*, 588, 1110
 Kuchner, M. J., & Stark, C. C. 2010, *AJ*, 140, 1007
 Kundu, M. R., Jackson, P. D., White, S. M., & Melozzi, M. 1987, *ApJ*, 312, 822
 Leto, G., Pagano, I., Linsky, J. L., Rodonò, M., & Umana, G. 2000, *A&A*, 359, 1035
 Liu, M. C. 2004, *Sci*, 305, 1442
 Liu, M. C., Matthews, B. C., Williams, J. P., & Kalas, P. G. 2004, *ApJ*, 608, 526
 Malhotra, R. 1995, *AJ*, 110, 420
 Metchev, S. A., Eisner, J. A., Hillenbrand, L. A., & Wolf, S. 2005, *ApJ*, 622, 451
 Morales, F. Y., Rieke, G. H., Werner, M. W., et al. 2011, *ApJL*, 730, 29
 Mustill, A. J., & Wyatt, M. C. 2009, *MNRAS*, 399, 1403
 Piétu, V., di Folco, E., Guilloteau, S., Gueth, F., & Cox, P. 2011, *A&A*, 531, L2
 Strubbe, L. E., & Chiang, E. I. 2006, *ApJ*, 648, 652
 Su, K. Y. L., Rieke, G. H., Stapelfeldt, K. R., et al. 2009, *ApJ*, 705, 314
 Trujillo, C. A., & Brown, M. E. 2001, *ApJL*, 554, 95
 van Leeuwen, F. 2007, *A&A*, 474, 653
 Weingartner, J. C., & Draine, B. T. 2001, *ApJ*, 548, 296
 White, S. M., Lim, J., & Kundu, M. R. 1994, *ApJ*, 422, 293
 Wilner, D. J., Andrews, S. M., & Hughes, A. M. 2011, *ApJL*, 727, 42
 Wilner, D. J., Andrews, S. M., MacGregor, M. A., & Hughes, A. M. 2012, *ApJL*, 749, 27
 Wyatt, M. C. 2003, *ApJ*, 598, 1321
 Wyatt, M. C. 2006, *ApJ*, 639, 1153
 Wyatt, M. C., Dermott, S. F., Telesco, C. M., et al. 1999, *ApJ*, 527, 918
 Zuckerman, B., Song, I., Bessell, M. S., & Webb, R. A. 2001, *ApJL*, 562, 87